



Site-density engineering of single-atomic iron catalysts for high-performance proton exchange membrane fuel cells

Feng Liu^{a,b}, Lei Shi^{a,b}, Xuanni Lin^a, Donglin Yu^{a,b}, Cai Zhang^a, Rui Xu^a, Dong Liu^{a,*}, Jieshan Qiu^a, Liming Dai^{c,*}

^a State Key Laboratory of Organic-Inorganic Composites, Beijing Advanced Innovation Center for Soft Matter Science and Engineering, College of Chemical Engineering, Beijing University of Chemical Technology, Beijing 100029, China

^b College of Materials Science and Engineering, Beijing University of Chemical Technology, Beijing 100029, China

^c Australian Carbon Materials Centre (A-CMC), School of Chemical Engineering, University of New South Wales, Sydney, NSW 2052, Australia

ARTICLE INFO

Keywords:

Oxygen reduction
Single-atom catalysts
N-doped porous carbons
Active site density
Fuel cell

ABSTRACT

The design and development of highly efficient non-precious metal single-atomic ORR catalysts for proton exchange membrane fuel cells (PEMFCs) are highly desirable but challenging. Herein, we report a novel polydopamine (PDA)-metal complex-assisted pyrolysis strategy for producing zeolitic imidazolate framework-derived catalysts with a hierarchically porous carbon support and highly exposed dense-FeN₄ sites (Z8@DA-FIP-950-C). The resultant Z8@DA-FIP-950-C catalyst shows remarkably enhanced performance for oxygen reduction reaction (ORR) with a half-wave potential ($E_{1/2}$) of 0.828 V in 0.1 M HClO₄ solution, which is close to commercial 20 wt% Pt/C catalyst. Impressively, the Z8@DA-FIP-950-C exhibits peak power densities of 982 and 454 mW cm⁻² in H₂/O₂ and H₂/air PEMFCs, respectively, which are superior to most of non-precious metal catalysts reported to date. In addition, we construct the quantitative relationship between the active site activity and ORR performance, and prove the dominating role of the FeN₄ site density to the observed excellent PEMFC performance. This work demonstrates a facile strategy to prepare the 3D hierarchically porous carbons with a maximized exposure of high-dense FeN₄ sites (without acid treatment), providing a useful guidance for the design and development of novel highly-efficient single-atom catalysts for the renewable energy applications.

1. Introduction

Having a high energy conversion efficiency with zero emission, PEMFCs show great potentials for renewable energy conversion in next-generation vehicles [1–4]. However, high cost of platinum (Pt)-based catalysts are commercially used to catalyze cathodic oxygen reduction reaction (ORR) for PEMFCs, which limit their large-scale applications [5,6]. Therefore, the development of low-cost platinum group metal free (PGM-free) catalysts is crucial for the practical applications of PEMFCs [7–10]. Recently, carbon-based catalysts incorporated with non-precious transition metals (M = Fe, Co, Ni, etc.) and nitrogen (M-N-C, especially Fe-N-C) have been recognized as one of the most promising catalysts due to their high ORR activity in acidic media [11–15]. Numerous studies have revealed that the atomic Fe-N_x (nitrogen-coordinated iron sites, x refers to the coordination number) moieties are the active sites for ORR [16–20]. Although many studies have reported various Fe-N-C catalysts with a high half-wave potential

tested by rotating disk electrode (RDE) method, their performance in a practical PEMFC still much poorer than that of the Pt/C catalysts due to the low utilization of Fe-N_x active sites and poor mass transport through the catalyst layer in the PEMFC [21–23]. Therefore, rationally designing hierarchically porous structures for promoting the mass transport and maximizing the exposure of the Fe-N_x active sites is recognized as one of the most promising strategies to improve the performance of PEMFCs [9, 24,25]. However, the preparation of atomically dispersed Fe-N-C catalysts with highly-dense active sites was challenging because the commonly-used high-temperature pyrolysis process usually leads to the generation of a significant amount of low-active sites or inactive Fe-based aggregates (Fe clusters and nanoparticles) when simply increasing the Fe concentration [26]. Furthermore, the catalysts containing Fe-based aggregates almost need to be washed by acid and pyrolyzed again to obtain the catalysts with only atomically dispersed Fe-N_x active sites [27–29]. Therefore, the preparation of atomically dispersed Fe-N-C catalysts with highly-dense atomic Fe-N_x sites by a

* Corresponding authors.

E-mail addresses: liudong@mail.buct.edu.cn (D. Liu), l.dai@unsw.edu.au (L. Dai).

<https://doi.org/10.1016/j.apcatb.2021.120860>

Received 30 July 2021; Received in revised form 22 September 2021; Accepted 25 October 2021

Available online 29 October 2021

0926-3373/© 2021 Elsevier B.V. All rights reserved.

facile strategy without acid treatment for high-performance PEMFCs is of significant importance.

Herein, we for the first time report a facile approach to the synthesis of highly-dense atomically-dispersed FeN₄ sites implanted in hierarchical porous carbons without acid treatment (denoted as Z8@DA-FIP-950-C) by pyrolysis of zinc-based zeolite imidazole framework (ZIF-8) particles coated by polydopamine (PDA) absorbed with Fe(II)-phenanthroline complex (FIP). During the pyrolysis process, the PDA coating can not only suppress the formation of Fe-based aggregates for efficient utilization of iron sources, but also facilitate the formation of mesopores and macropores, creating carbon-based catalysts with abundant defective-edge and FeN₄ sites. The as-prepared Fe-N-C catalyst possessed a 3D hierarchically porous carbon skeleton, which included enriched triple-phase boundaries for boosting mass transport and highly exposed FeN₄ sites, leading to high ORR activity even in acidic electrolyte. Moreover, the newly-developed Fe-N-C catalysts with different densities of FeN₄ sites can be used for studying the quantitative relationship between the active site and ORR performance. The optimized Fe-N-C catalysts with the maximized exposure of atomic FeN₄ sites exhibited remarkably enhanced ORR activity in acid media, and demonstrated unusually high performance in practical H₂/air fuel cells.

2. Experimental section

2.1. Preparation of ZIF-8 nanocrystals

In a typical procedure, 2.23 g of Zn(NO₃)₂·6H₂O was dissolved in 50 ml of methanol to form a clear solution, into which 50 ml of methanol solution containing 2.46 g 2-methylimidazole was poured quickly, followed by vigorous stirring for 5 h. The white precipitates were centrifuged, washed several times with methanol, and finally dried overnight under vacuum at 80 °C.

2.2. Preparation of Z8@DA-FIP-950-C

Typically, 200 mg of ZIF-8 was dispersed in a mixed solution of ethanol (30 ml) and water (30 ml) by ultrasound for 2 h. 15 mg of dopamine and 12 mg of Pluronic F127 were then added into above mixture solution with vigorous magnetic stirring. Thereafter 0.6 ml of FIP ethanol solution (50 mg ml⁻¹, prepared by dissolving ferrous acetate (Fe(Ac)₂) and 1,10 phenanthroline (phen) with molar ratio of 1:3 in ethanol) were added drop-wise into the above dispersion with vigorous stirring. Different volumes (0.2, 0.3, 0.4, 0.5 and 0.6 ml) of FIP ethanol solution were added while the subsequent steps remained unchanged. After stirring for 30 min, 0.4 ml of ammonia solution was added to induce the value of the mixture solution pH reached to 8.5. The reaction proceeded under magnetic stirring for 24 h at room temperature, and contacted with air simultaneously. The products were collected by centrifugation and washed with deionized water and ethanol three times, and finally dried in vacuum at 60 °C overnight. The obtained product was denoted as Z8@DA-FIP. Hierarchically porous Fe-N-C single-atom catalysts could be produced after pyrolysis from Z8@DA-FIP. The precursor Z8@DA-FIP was firstly heated to 350 °C with a heating rate of 2 °C min⁻¹, and maintained at the temperature of 350 °C for 2 h under argon atmosphere. After that, the temperature was further increased to 950 °C with a heating rate of 5 °C min⁻¹, and kept for 2 h. When the temperature dropped to 800 °C, ammonia (70 ml min⁻¹) was introduced into the tube, and the furnace was kept at this temperature for 8 min. Subsequently, the ammonia was switched to argon, and the furnace was naturally cooled to room temperature. The final product was denoted as Z8@DA-FIP-950-C.

2.3. Preparation of Z8@FIP-950-C, Z8@DA-950-C, and DA-FIP-950-C

For Z8@FIP-950-C and Z8@DA-950-C, the addition of dopamine and FIP ethanol solution did not be performed in the process of the

preparation of Z8@DA-FIP, respectively. The following pyrolysis step was identical to Z8@DA-FIP-950-C. The final obtained Z8@FIP-950-C catalyst was treated with HCl (2 M) followed by washing with distilled H₂O to remove the Fe-based nanoparticles and subjected to a second heat treatment. For DA-FIP-950-C, 215 mg of dopamine and 12 mg of Pluronic F127 were added into a mixed solution of ethanol (30 ml) and water (30 ml) with magnetic stirring. The following procedures were identical to the preparation of Z8@DA-FIP-950-C.

2.4. Physical characterization

Scanning electron microscopy (SEM) images were obtained from TESCAN MAIA3 scanning electron microscope. Transmission electron microscopy (TEM), high resolution transmission electron microscopy (HRTEM), selected area electron diffraction (SEAD), high-annular dark-field scanning TEM (HAADF-STEM), and EDS were conducted on a JEOL JEM-2200FS transmission electron microscope. Aberration-corrected High-angle annular dark-field scanning transmission electron microscopy (HAADF-STEM) images and electron energy loss spectroscopy (EELS) were performed with a JEOL JEM-ARM 200F transmission electron microscope with a probe corrector operated at 200 kV. The X-ray absorption fine structure spectra (XAFS) spectra at the Fe K-edge were measured at 1W1B station in Beijing Synchrotron Radiation Facility (BSRF), operated at 2.5 GeV with a maximum current of 250 mA). The spectra of samples were recorded in fluorescence excitation mode using a Lytle detector. The spectra of Fe foil and Fe₂O₃ were used as references, and recorded in a transmission mode using ionization chamber. The crystal phases of the samples were characterized by a Bruker D2 Phaser X-ray diffractometer with a Cu K α radiation source (30 kV, 10 mA). Raman spectra were recorded using a Horiba LabRAM HR Evolution Raman spectrometer operating with a laser wavelength of 532 nm. The nitrogen adsorption and desorption isotherms were studied by using a Micrometrics ASAP 2460 Specific surface and porosity analyzer. The specific surface area and pore size distribution were calculated from the nitrogen adsorption-desorption isotherms. X-ray photoelectron spectroscopy (XPS) measurements were carried out on a Kratos AXIS SUPRA X-ray photoelectron spectrometer with an Al K α radiation (15 kV, 10 mA). ¹³C solid state nuclear magnetic resonance (ssNMR) spectra were recorded on a Bruker AVANCE III 400 spectrometer operating at B₀ field of 7.05 T with ¹³C Larmor frequency of 75.4 MHz.

2.5. Electrochemical measurements

The oxygen reduction reaction (ORR) activities of catalysts were measured by a CHI Electrochemical workstation (model 760c) with a standard three-electrode system at room temperature. The catalyst-coated glassy carbon rotating disk electrode (RDE, 5 mm in diameter) or rotating ring-disk electrode (RRDE, disk outer diameter, ring inner diameter and ring outer diameter are 5.61 mm, 6.25 mm, and 7.92 mm, respectively) was used as the working electrode, an Ag/AgCl electrode in saturated KCl solution was used as the reference electrode, and Pt wire was used as counter electrode. All of the potentials reported in this paper were calibrated to the reversible hydrogen electrode. To prepare a homogeneous catalyst ink, 5 mg of catalyst was dispersed in a solution of 245 μ l of deionized water, 245 μ l of isopropanol and 10 μ l of a Nafion solution (5 wt%, Alfa Aesar D521) under sonication for 2 h. Then 15 μ l of catalyst ink were loaded onto the glassy carbon and dried in air. A Pt/C (20 wt% of Pt, Johnson Mattery HiSPEC) catalyst with a loading of 20 μ g cm⁻² was used as a reference. Cyclic voltammetry (CV) measurements were performed in N₂- or O₂- saturated 0.1 M HClO₄ solution with a sweep rate of 50 mV s⁻¹. Linear scan voltammetry (LSV) tests were carried out in O₂-saturated 0.1 M HClO₄ solution with a scan rate of 5 mV s⁻¹. Four-electron selectivity during the ORR was determined by measuring LSV curves on RDE at various rotating speeds (400, 625, 900, 1225, 1600, and 2025 rpm). The corresponding electron transfer

number was determined from the slope of the linear line according to the following Koutecký-Levich (K-L) equation:

$$\frac{1}{J} = \frac{1}{J_L} + \frac{1}{J_K} = \frac{1}{B\omega^{1/2}} + \frac{1}{J_K}$$

$$B = 0.62nF(D_0)^{2/3}(\nu)^{-1/6}C_0 \quad (1)$$

where J , J_L , J_K are the measured current density, diffusion-limiting current density, and kinetic current density, respectively. ω is the angular velocity of the disk ($\omega = 2\pi N$, N is the rotation speed), n is the electron transfer number, F is the Faraday constant ($F = 96,485 \text{ C mol}^{-1}$), D_0 is the diffusion coefficient of oxygen ($D_0 = 1.93 \times 10^{-5} \text{ cm}^2 \text{ s}^{-1}$, 0.1 M HClO_4), C_0 is the bulk concentration of oxygen ($C_0 = 1.2 \times 10^{-6} \text{ mol cm}^{-3}$, 0.1 M HClO_4), ν is the kinetic viscosity of the electrolyte ($\nu = 0.01 \text{ cm}^2 \text{ s}^{-1}$). The electron transfer number (n) and the yield of H_2O_2 were calculated from the RRDE measurement based on the disk current (I_d) and ring current (I_r) via the following equations:

$$n = 4 \times \frac{I_d}{I_d + I_r/N} \quad (2)$$

$$\text{H}_2\text{O}_2\% = 200 \times \frac{I_r}{(I_r + NI_d)} \quad (3)$$

where $N = 0.37$ is the current collection efficiency of Pt ring.

The gravimetric active site density (MSD) and turnover frequency (TOF) of the catalysts were obtained via electrochemical stripping experiments [10,30]. Briefly, CV measurements were performed in Ar- or O_2 -saturated pH 5.2 acetate buffer from sodium acetate and glacial acetic acid. Then the catalysts were poisoned by NaNO_2 , and Nitrite stripping was carried out in the region of 0.2 to -0.3 V versus the reversible hydrogen electrode. CV curves measured in Ar-saturated acetate buffer and RDE polarization curves tested in O_2 -saturated acetate buffer were recorded before, during and after the nitrite absorption. Q_{strip} (excess coulometric charge associated with the stripping peak) could be proportional to the MSD, and the TOF was associated with the difference of j_k (kinetic current density) before and after nitrite absorption, MSD and TOF were calculated from the following equations:

$$\text{MSD} (\text{mol g}^{-1}) = \frac{Q_{\text{strip}} (C \text{ g}^{-1})}{n_{\text{strip}} F (C \text{ mol}^{-1})} \quad (4)$$

$$\text{TOF} (\text{s}^{-1}) = \frac{n_{\text{strip}} \Delta j_k (\text{mA cm}^{-2})}{Q_{\text{strip}} (C \text{ g}^{-1}) L_C (\text{mg cm}^{-2})} \quad (5)$$

where n_{strip} ($= 5$) is the number of electrons associated with the reduction of one adsorbed nitrosyl per FeN_4 site. The loading of catalyst (L_C) is 0.27 mg cm^{-2} .

2.6. MEA fabrication and fuel cell measurement

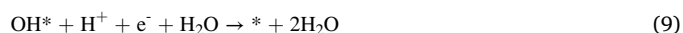
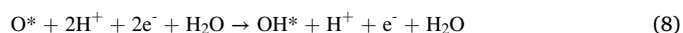
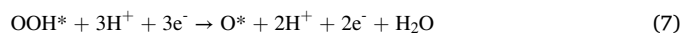
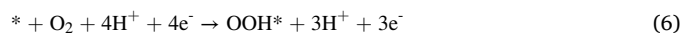
20 mg of catalyst was homogeneously dispersed in a mixture solution containing 1000 μl isopropanol, 500 μl deionized water, and 400 mg Nafion (5 wt%) solution. The obtained catalyst ink was then brushed onto the SGL 29BC gas diffusion layer with an effective area of 5 cm^2 until the loading amount reached 3 mg cm^{-2} , which served as the cathode for PEMFC. As for the anode, Pt/C (40 wt% of Pt, Johnson Mattery HiSPEC) was used with a loading of $\sim 0.4 \text{ mg}_{\text{Pt}} \text{ cm}^{-2}$. The membrane electrode assembly (MEA) was obtained by hot pressing as-prepared cathode and anode onto the two sides of a Nafion 211 membrane (DuPont) at 130°C for 2 min under a pressure of 0.6 MPa. The H_2/O_2 or /air PEMFC test was performed on a fuel cell test station (Arbin FCTS) at stated back pressure, 80°C and 100% relative humidity (RH). The flow rate of H_2 and O_2 (or air) was 300 and 400 sccm, respectively. The η_{mt} was determined by dividing the difference of a conceptual

polarization curve with ohmic resistances and mass transport corrected and the iR-free polarization curve [20].

2.7. Computational details

Periodic density functional theory (DFT) calculations were carried out using the DMol3 module in the Material Studio 8.0 software package [31,32]. The generalized gradient approximation (GGA), with Perdew-Burke-Ernzerhof (PBE) functions were used for the exchange and correlation in the Kohn-Sham equations [33]. The k point grids were set as $2 \times 2 \times 1$ for the Brillouin zone and a large vacuum slab of 15 \AA is inserted in z direction for surface isolation to prevent interaction between two neighboring surfaces. The convergence threshold for the iteration in self-consistent-field (SCF) is set to be 10^{-5} eV .

The ORR proceeds in $4e^-$ pathway are shown as follows [34]:



where $*$ refers to an active site on the catalysts surface.

The reaction Gibbs free energy changes (ΔG) were calculated by the following equation:

$$\Delta G = \Delta E + \Delta ZPE - T\Delta S + \Delta G_{\text{pH}} + \Delta G_U \quad (10)$$

where ΔE is obtained directly from DFT calculation results, ΔZPE is the correction of zero point vibration energy (ZPE), T is the room temperature of 298.15 K , and ΔS is the correction for entropy. $\Delta G_{\text{pH}} = -k_B T \ln[H^+] = \text{pH} \times k_B T \ln 10$ [35], is the change of free energy owing to the effect of pH value of the electrolyte. $\Delta G_U = -neU$, is the effect of the electrons transfer in the electrode and the electrode potential contribution to ΔG .

3. Results and discussion

3.1. Catalyst preparation and structure characterization

The facile synthetic procedure for atomically dispersed FeN_4 sites in 3D hierarchical porous carbons (Z8@DA-FIP-950-C) could be divided into three steps, as illustrated in Fig. 1. Firstly, ZIF-8 was prepared via a general approach by reaction of 2-methylimidazole (2-MIM) with $\text{Zn}(\text{NO}_3)_2$ in methanol solution at room temperature for 5 h [22]. Subsequently, dopamine (DA) with $\text{Fe}(\text{II})$ -phenanthroline complex could be self-polymerized onto the surface of ZIF-8 particles, producing polydopamine (PDA)/ $\text{Fe}(\text{II})$ -phenanthroline complex coated ZIF-8 particles (Z8@DA-FIP). The positively charged $\text{Fe}(\text{II})$ -phenanthroline complex are easily absorbed into the PDA chains with negative charge, which can uniformly coat onto the surface of ZIF-8 in the Z8@DA-FIP. During the Z8@DA-FIP formation, the deprotonation equilibrium of 2-MIM in ZIF-8 was disordered by the protons released from DA, and Zn^{2+} released from ZIF-8 tend to coordinate with phenolic hydroxyl groups of PDA [36]. Finally, Z8@DA-FIP were carbonized and transformed into 3D hierarchical porous carbon decorated with dense FeN_4 sites (Z8@DA-FIP-950-C). The hierarchically porous structure of Z8@DA-FIP-950-C was produced by the release of Zn^{2+} and 2-MIM without coordination during pyrolysis of Z8@DA-FIP. The release of Zn^{2+} and 2-MIM during the pyrolysis process can not only increase the porosity, but also expose a number of defective-edge FeN_4 sites and carbon defects, both contributing to the acidic ORR activity for Z8@DA-FIP-950-C [37–40].

The morphologies of the Z8@DA-FIP precursor and Z8@DA-FIP-950-C were characterized by scanning electron microscopy (SEM) and transmission electron microscopy (TEM). Fig. S1a,c show that Z8@DA-

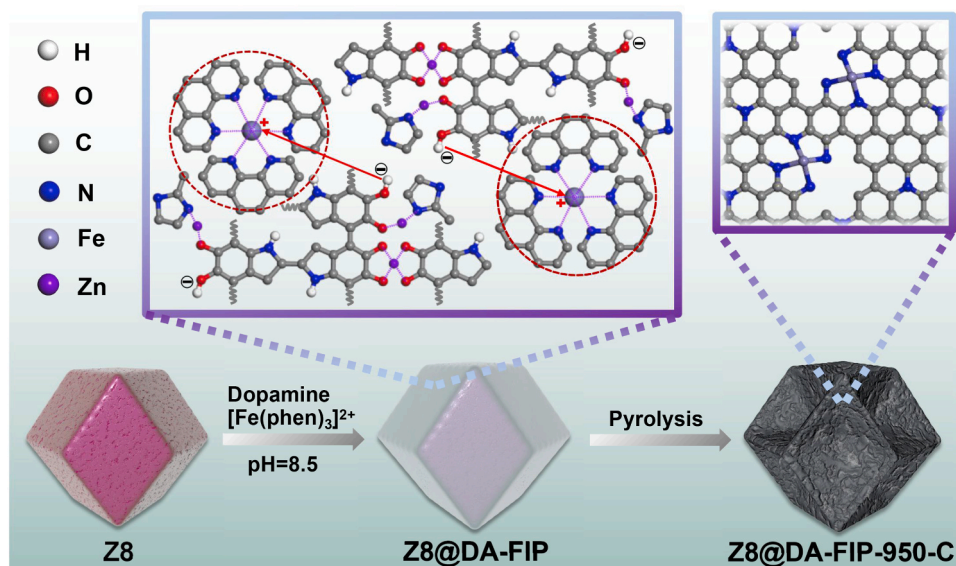


Fig. 1. Illustration of the synthesis of Z8@DA-FIP-950-C: a) polydopamine was coated over the surface of ZIF-8 (Z8) through self-polymerization of dopamine, and positively charged Fe (II)-phenanthroline (FIP) complex was tend to absorb into the polydopamine chains with negative charge (pH = 8.5), forming Z8@DA-FIP; b) The pyrolysis of Z8@DA-FIP at 950 °C leads to the formation of Z8@DA-FIP-950-C.

FIP (100 nm) possesses a uniform dodecahedral shape with rough surfaces and an obvious PDA layer. By comparison, Z8@FIP without PDA coating displays smooth surfaces (Fig. S2a,c). After carbonizing, a obvious concave morphology with sharp edges was observed for Z8@DA-FIP-950-C (Figs. 2a,b and S1b,d), which can be ascribed to the anisotropic thermal shrinkage of ZIF-8 induced by carbon shell derived from the PDA layer [9,41]. More importantly, distinct interior cavities were observed for Z8@DA-FIP-950-C (inset in Fig. 2b).

The porosity of the obtained carbon was further evaluated by the nitrogen adsorption-desorption isotherms. As shown in Fig. S3a, the large adsorption capacity of Z8@DA-FIP-950-C at low relative pressures indicates the existence of abundant micropores [42]. Z8@DA-FIP-950-C exhibits more obvious adsorption hysteresis loop than Z8@FIP-950-C, reflecting the presence of more mesopores and macropores in Z8@DA-FIP-950-C than in Z8@FIP-950-C [33]. Pore volume analysis reveals that Z8@DA-FIP-950-C exhibits a higher total pore volume than that of Z8@FIP-950-C (Table S1). The pore size distribution curves in Fig. S3b confirms the existence of hierarchical micropores, mesopores and macropores in Z8@DA-FIP-950-C. The abundant mesopores and macropores are expected to be beneficial for fast mass transport in the PEMFC. Such plenty of generated cavities and holes imply the richness of more defects in the Z8@DA-FIP-950-C catalyst, as also confirmed by a high I_D/I_G ratio for Z8@DA-FIP-950-C (1.03) compared to that of Z8@FIP-950-C (0.96) from the Raman spectra (Fig. S4) [43].

Homogenous absorption of FIP occurred at the PDA chains, which could effectively suppress the aggregates of FIP multimolecular complex, thus benefiting for in-situ generation of homogeneously atomic Fe-N_x moieties without the formation of Fe-based nanoparticles during subsequent pyrolysis process. TEM, selected area electron diffraction (SAED) and X-ray diffraction (XRD) were conducted to confirm that the Z8@DA-FIP-950-C and Z8@FIP-950-C catalysts did not include crystalline Fe species (Figs. 2c, S5, and S6). By contrast, the Z8@FIP-950-C catalyst without acid treatment suffered from severe Fe agglomeration, and even several carbon nanotubes (CNTs) existed on the surface of the irregular polyhedron, which were catalyzed by the Fe-based nanoparticles during the carbonization process (Figs. S2b, d–f, and S7) [44]. Furthermore, atomically dispersed Fe atoms in the carbon skeleton of Z8@DA-FIP-950-C can be directly observed and confirmed by aberration-corrected high-angle annular dark-field scanning TEM (AC HAADF-STEM) characterization (Figs. 2d,e, S8, and S9) [45], which

display isolated atomic-scale bright dots, corresponding to isolated Fe atoms. However, the Z8@FIP-950-C catalyst without acid treatment showed obvious Fe clusters (Fig. S10a,b), which can be removed by acid treatment (Fig. S10c,d). The HAADF-STEM and energy-dispersive X-ray spectroscopy (EDS) mapping images exhibit uniform elemental dispersion of C, N, and Fe elements over Z8@DA-FIP-950-C (Fig. 2f).

X-ray photoelectron spectroscopy (XPS) was employed to characterize the surface chemical composition and structure of Z8@DA-FIP-950-C and Z8@FIP-950-C. The XPS survey spectra confirm that both Z8@DA-FIP-950-C and Z8@FIP-950-C are mainly composed of C, N, O, and Fe elements (Figs. S11a and S12a), and the surface Fe contents of Z8@DA-FIP-950-C and Z8@FIP-950-C are 3.04 and 1.47 wt%, respectively (Table S2). The high-resolution N 1s curves of the two catalysts can be deconvoluted into pyridinic-N (398.2 eV), Fe-N_x (398.9 eV), pyrrolic-N (399.5 eV), graphitic-N (401.0 eV), and oxidized-N bonded species (404.0 eV) (Figs. S11b and S12b) [46]. It is worth noting that Fe-N_x bonding at around 398.9 eV indicated that Fe atoms have a strong interaction with the neighboring doped N. Z8@DA-FIP-950-C exhibits a higher percentage of Fe-N_x species than that of Z8@FIP-950-C, as shown in Figs. S11d and S12d, implying that the Z8@DA-FIP-950-C with a 3D hierarchical porous structure possesses a higher density of atomic Fe-N_x moieties.

To investigate the chemical state and metal coordination environment of Z8@DA-FIP-950-C, the X-ray absorption near-edge structure (XANES) and extended X-ray absorption fine structure (EXAFS) measurements were carried out [47]. As shown in Fig. 2g, the Fe K-edge profile of Z8@DA-FIP-950-C in XANES located between those of Fe foil and Fe₂O₃ and next to that of Fe₂O₃, suggesting that the valence state of Fe in Z8@DA-FIP-950-C is close to that of Fe (III) [48]. Fig. 2h shows that the Fourier-transformed (FT) Fe K-edge EXAFS curve for Z8@DA-FIP-950-C, which only presents a prominent peak at approximately 1.5 Å attributable to the Fe-N configuration [49]. An Fe-Fe peak at approximately 2.2 Å is not detected from the Z8@DA-FIP-950-C FT EXAFS curve, which further clearly reveals that Fe are atomically dispersed and stabilized by nitrogen. The exact coordination structure of Fe atom in Z8@DA-FIP-950-C can be attained by the EXAFS fitting [50, 51]. According to the fitting curves and parameters given in Figs. 2i, S13 and Table S3, the coordination number of Fe-N can be deduced to be four, suggesting the formation of FeN₄ configuration in the carbon support [52].

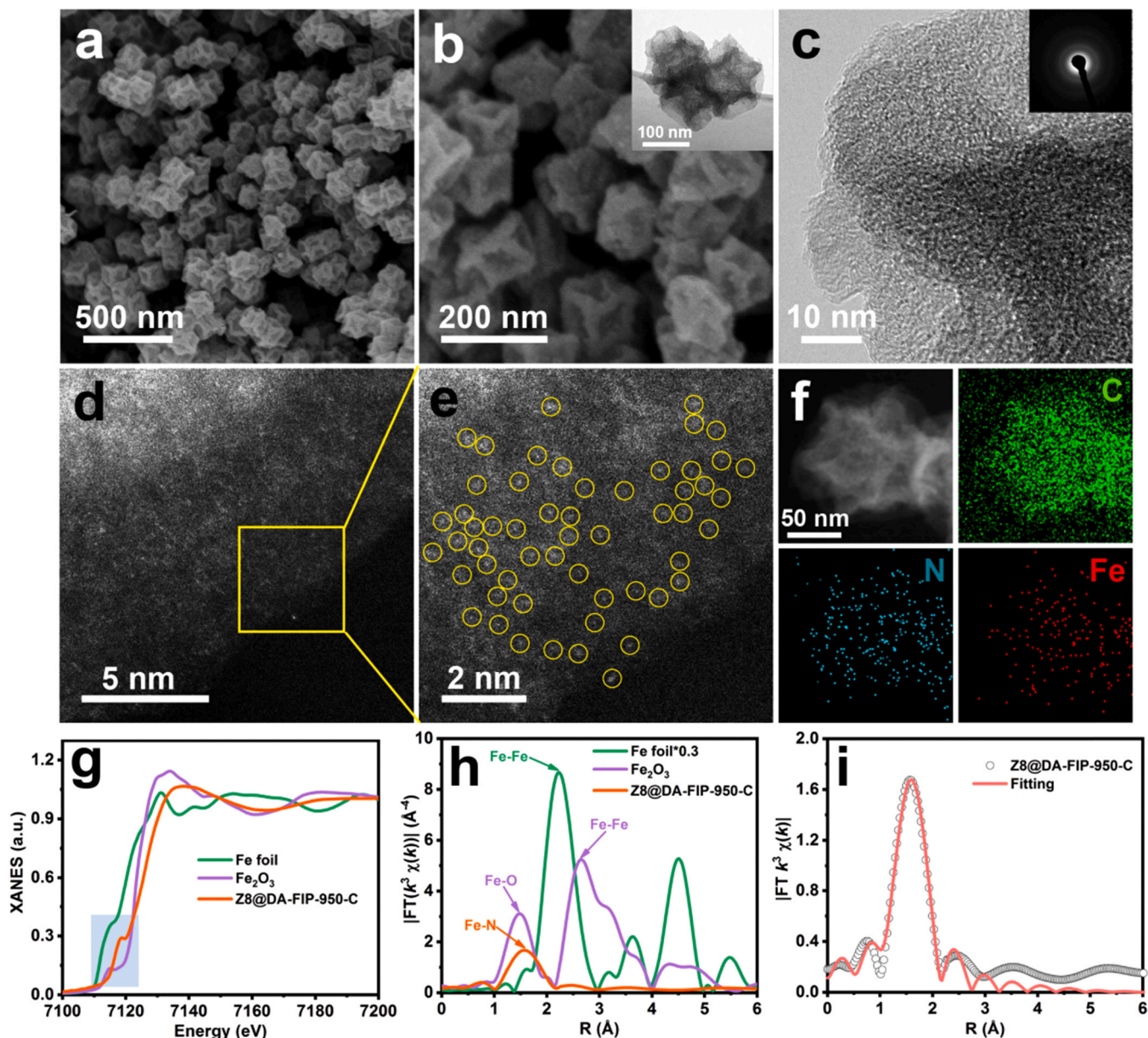


Fig. 2. a, b) SEM and TEM, c) HRTEM (inset in c: corresponding SAED pattern) and d, e) AC HAADF-STEM images of Z8@DA-FIP-950-C. f) HAADF-STEM and corresponding EDS mapping images of C, N, and Fe elements of Z8@DA-FIP-950-C. g) Fe K-edge XANES and h) FT Fe K-edge EXAFS spectra of Z8@DA-FIP-950-C and references. i) FT-EXAFS R-space fitting curve of Z8@DA-FIP-950-C.

3.2. Electrocatalytic performance of ORR

To evaluate the ORR activity of the as-prepared catalysts, we performed the half-cell tests (i.e., the rotating disk electrode (RDE) measurements) in O_2 -saturated 0.1 M $HClO_4$. For the LSV curves shown in Figs. S14–S18, the optimal catalysts of Z8@DA-FIP-950-C were prepared by regulating the amounts of metal precursors ($Fe(AC)_2$ and $Fe(AC)_2$ -phenanthroline (FIP) complex), FIP, and DA. As revealed in Fig. 3a, Z8@DA-FIP-950-C shows the highest activity with a high onset potential (E_0) of 0.96 V and a half-wave potential ($E_{1/2}$) of 0.828 V, both of which are close to those of the commercial Pt/C ($E_0 = 0.98$ V, $E_{1/2} = 0.859$ V), but higher than those of most of previously-reported non-precious metal catalysts (Fig. 3h and Table S7). The $E_{1/2}$ for the reference sample of DA-free Fe-N-C sample (Z8@FIP-950-C) is 0.776 V, which is 52 mV less than that of Z8@DA-FIP-950-C. The excellent ORR performance observed for Z8@DA-FIP-950-C could be attributed to the high-density of Fe-N₄ active sites and hierarchically porous structure. The prepared metal-free

N-doped carbon (Z8@DA-950-C) derived from ZIF-8@polydopamine through volatilization of Zn at a boiling point of 907 °C with no addition of Fe source [53,54]. Z8@DA-950-C showed a lower $E_{1/2}$ (0.547 V) than that of Z8@DA-FIP-950-C, implying that the Fe-N₄ sites possessed a higher ORR activity than that of the N-C sites. Many other literatures also reported that M-N-C catalysts exhibited better experimental ORR performance than that of N-C catalysts, and DFT calculations revealed the higher intrinsic ORR activity for M-N_x sites than that of N-C sites [9, 26,55,56]. In addition, the ZIF-8 free Fe-N-C carbon catalyst (DA-FIP-950-C) derived from polydopamine/Fe(II)-phenanthroline complex showed also a lower $E_{1/2}$ (0.604 V) than those of Z8@DA-FIP-950-C and Z8@FIP-950-C, indicating that ZIF-8 matrix with abundant micropores is the suitable material for constructing the carbon-based single-atomic catalysts for efficient ORR [49,57,58].

Fig. 3b shows that the kinetic current density (J_k) of 21.342 mA cm^{-2} at 0.8 V for Z8@DA-FIP-950-C is much higher than those of Z8@FIP-950-C (2.932 mA cm^{-2}), Z8@DA-950-C

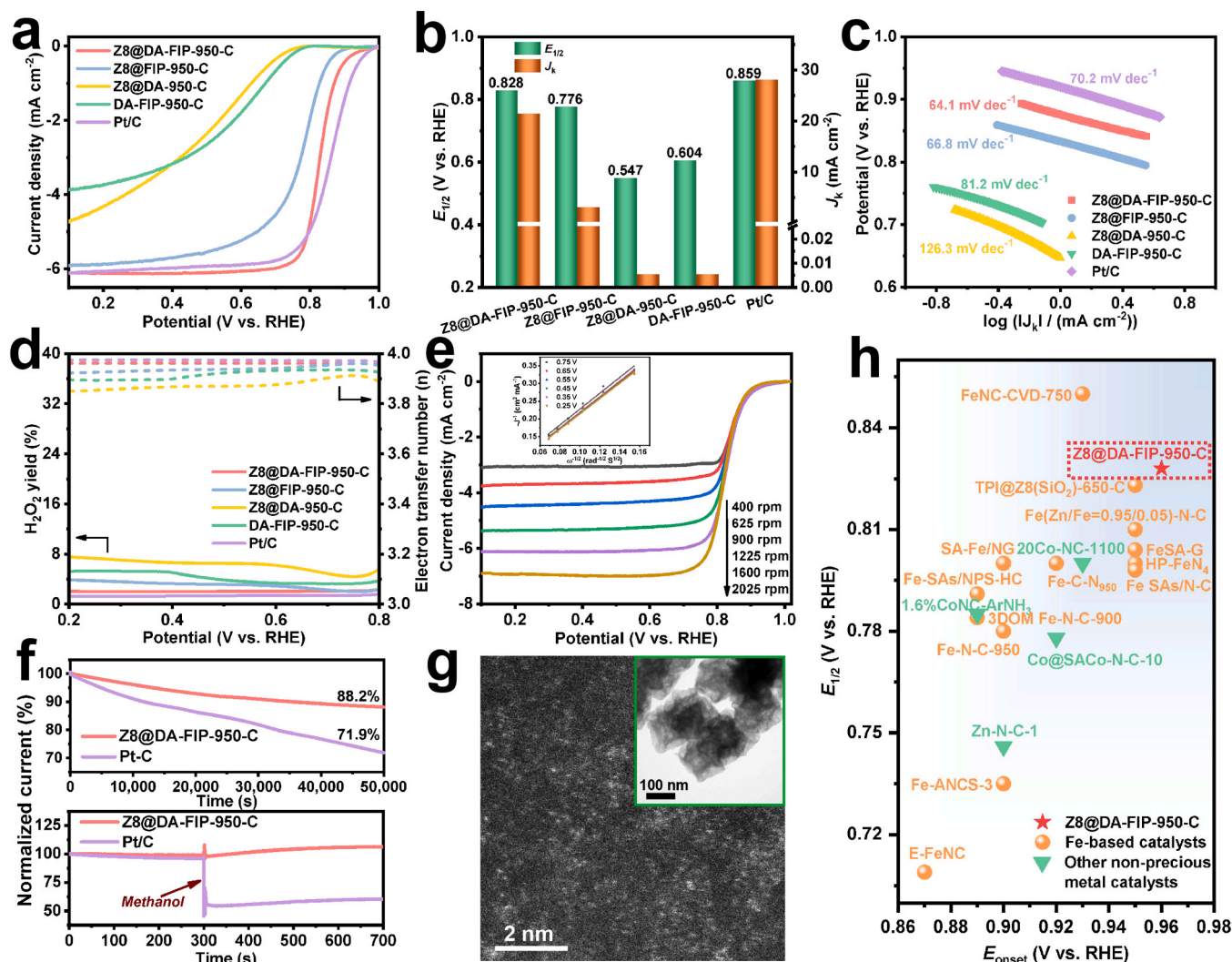


Fig. 3. a) RDE polarization curves of Z8@DA-FIP-950-C, Z8@FIP-950-C, Z8@DA-950-C, DA-FIP-950-C, and Pt/C in O₂-saturated 0.1 M HClO₄ solution with a scan rate of 5 mV S⁻¹ and a rotation rate of 1600 rpm. b) Comparison of $E_{1/2}$ and J_k at 0.8 V for different catalysts. c) Corresponding Tafel plots from RDE polarization curves, and d) number of transferred electrons (n) and yields of H₂O₂ of various catalysts. e) RDE polarization curves of Z8@DA-FIP-950-C at various rotation rates; inset shows the corresponding K-L plots. f) Stability evaluation (top) and methanol resistance test (bottom) of Z8@DA-FIP-950-C and Pt/C. g) TEM and HAADF-STEM image of Z8@DA-FIP-950-C after the ADT test. h) Comparison of E_{onset} and $E_{1/2}$ of Z8@DA-FIP-950-C and the previously reported Fe-based catalysts and other non-precious metal catalysts in Table S7.

(0.005 mA cm⁻²) and DA-FIP-950-C (0.005 mA cm⁻²), and close to that of Pt/C (28.060 mA cm⁻²) in 0.1 M HClO₄. This is consistent with a smaller Tafel slope of 64.1 mV dec⁻¹ for Z8@DA-FIP-950-C compared with that of Pt/C (70.2 mV dec⁻¹) (Fig. 3c). Moreover, the ORR pathways and H₂O₂ generation during ORR process were studied by rotating ring-disk electrode (RRDE) tests. Fig. 3d shows the number of transferred electrons (n) and H₂O₂ yield for various as-prepared catalysts, indicating that the n for both Z8@DA-FIP-950-C and Pt/C are close to 4.0, and that the H₂O₂ yields over the potential range from 0.80 to 0.20 V are consistently below 2%. The number of transferred electrons for Z8@DA-FIP-950-C can also be calculated from the slopes of Koutecký-Levich (K-L) plots, and the value of n is close to the ideal value of 4.0 at the potential range from 0.75 to 0.25 V (Fig. 3e). These results suggest that the Z8@DA-FIP-950-C exhibits a four-electron ORR process in acidic medium. The K-L plots of both Z8@DA-FIP-950-C and Z8@FIP-950-C present parallel lines, suggesting the first-order reaction kinetics (Fig. S19) [59]. Notably, Z8@DA-FIP-950-C shows a better long-term stability than that of the commercial Pt/C in 0.1 M HClO₄, as confirmed by the slower decay rate in the chronoamperometry measurements (Fig. 3f, top) and lower decay in $E_{1/2}$ during the accelerated

durability test (ADT) (Fig. S20). After the ADT test, no obvious morphological changes were observed for Z8@DA-FIP-950-C, and Fe remains as isolated atoms without obvious aggregation (Fig. 3g). In addition, the Z8@DA-FIP-950-C also exhibits an excellent tolerance to methanol crossover in acidic medium (Fig. 3f, bottom), as evidence by almost no change in the current density of Z8@DA-FIP-950-C after methanol injection, while the Pt/C catalyst suffered a significant decrease in current density due to methanol poisoning (Fig. 3f, bottom). Clearly, therefore, Z8@DA-FIP-950-C exhibits an excellent stability in acidic medium.

3.3. The quantitative relationship of the active site and the catalytic activity

To demonstrate potential applications for the Z8@DA-FIP-950-C, we assembled the catalyst into a membrane electrode assembly (MEA) for PEMFCs. Fig. 4a schematically shows the working principle of the PEMFCs, and a digital photograph of the single cell assembly could be seen in Fig. S21. Fig. 4b shows the polarization and power density curves. With O₂ as an oxidant, the Z8@DA-FIP-950-C catalyst exhibits

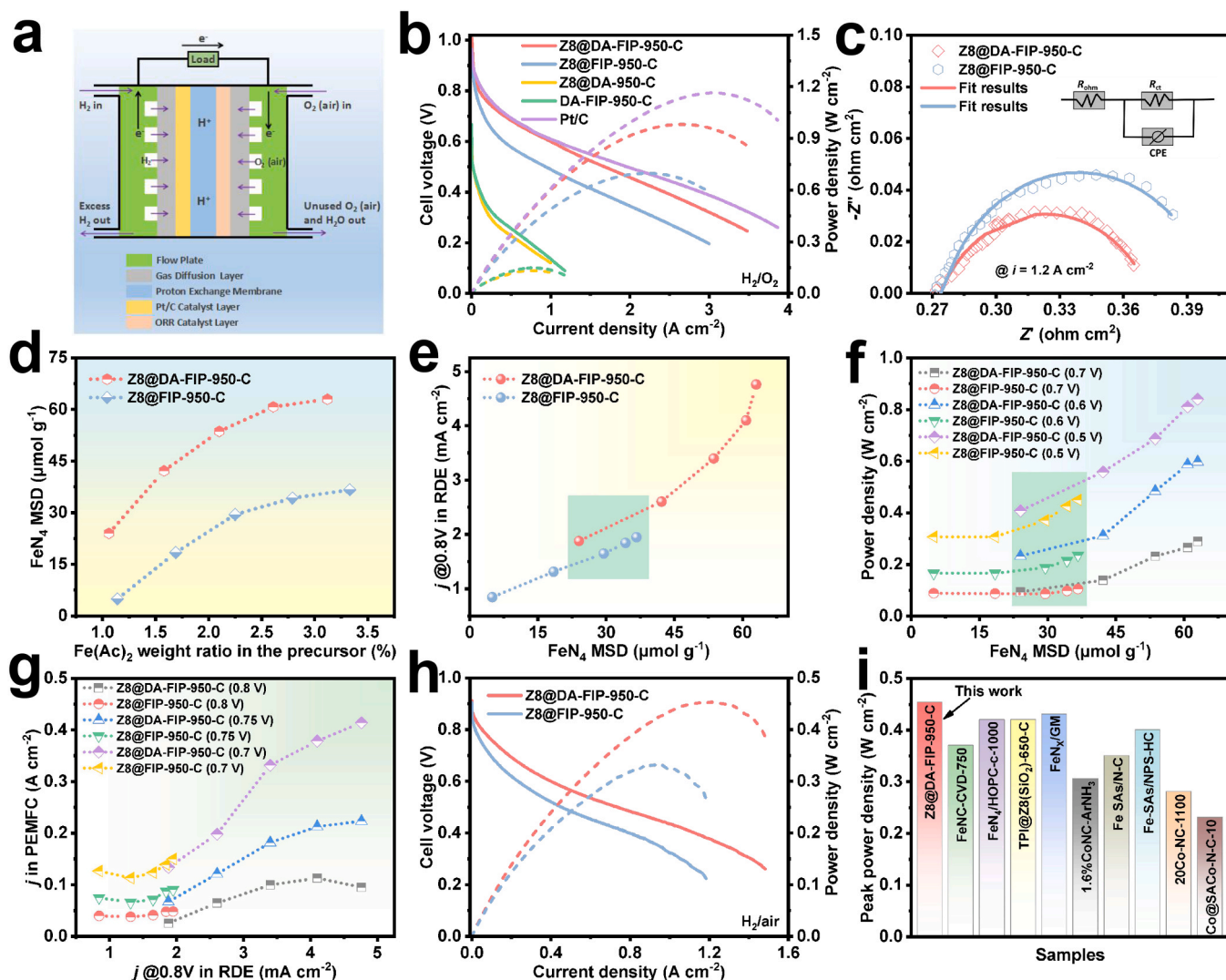


Fig. 4. a) Schematic of the assembled fuel cell used for PEMFC. b) PEMFC polarization and power density curves of the indicated cathode catalysts. Test conditions: cathode loading of 3 mg cm^{-2} for the indicated platinum-free catalysts and $0.4 \text{ mg}_{\text{Pt}} \text{ cm}^{-2}$ for Pt/C, anode loading of $0.4 \text{ mg}_{\text{Pt}} \text{ cm}^{-2}$ for Pt/C, 2 bar H_2/O_2 at flow rates of 300 or 400 ml min^{-1} , Nafion 211 membrane, 80°C , 100% relative humidity. c) Nyquist plots for PEMFC of Z8@DA-FIP-950-C and Z8@FIP-950-C cathode catalysts at the current density of 1.2 A cm^{-2} , the inset shows the equivalent circuit model. Z' and $-Z''$ are the real and imaginary parts of the impedance. d) The plot of FeN_4 MSD of Z8@DA-FIP-950-C and Z8@FIP-950-C as a function of $\text{Fe}(\text{Ac})_2$ content in the precursors. e) The plot of current densities (j) at 0.8 V measured by RDE in O_2 -saturated 0.1 M HClO_4 as a function of FeN_4 MSD. f) The correlation between FeN_4 MSD and PEMFC power densities at 0.5, 0.6, and 0.7 V. g) The correlation between ORR activity and PEMFC current densities (j) at 0.7, 0.75, and 0.8 V. h) Polarization and power density plots of PEMFC with Z8@DA-FIP-950-C and Z8@FIP-950-C under 1 bar H_2/air at flow rates of 300 or 400 ml min^{-1} . i) The comparison of peak power density in H_2/air PEMFC between Z8@DA-FIP-950-C and those from other reports.

current densities of 0.68 and 3.46 A cm^{-2} at 0.65 and 0.25 V, respectively, significantly outperformed the Z8@FIP-950-C, Z8@DA-950-C and DA-FIP-950-C catalysts. The maximum power density of the Z8@DA-FIP-950-C-based PEMFC reaches to 982 mW cm^{-2} at a back pressure of 2 bar, outperformed most of the previously-reported non-precious metal catalysts (Table S8). The corresponding Tafel plots demonstrate a rate of 47.8 mV dec^{-1} for Z8@DA-FIP-950-C, which is lower than 93.4 mV dec^{-1} and 68.6 mV dec^{-1} for Z8@FIP-950-C and Pt/C, respectively (Fig. S22), suggesting a superior rate for the electrochemical reaction in the PEMFC cell and an excellent ORR kinetics in the half-cell. Furthermore, Z8@DA-FIP-950-C presents a higher stable open circuit voltage (OCV) (1.012 V) than that of Z8@FIP-950-C (0.965 V) (Fig. S23). The mass transfer ability of Z8@DA-FIP-950-C and Z8@FIP-950-C can be evaluated by the mass-transport overpotential (η_{mt}) at a high current density of 1.2 A cm^{-2} extracted from the polarization curves (Fig. S24). Z8@DA-FIP-950-C with abundant meso/macropores showed a η_{mt} of 46 mV, which was lower than the corresponding value

of 84 mV for Z8@FIP-950-C with less meso-/macro-pores. This indicates that the 3D hierarchical porous structure with meso/macropores greatly enhanced the mass transfer for the Z8@DA-FIP-950-C catalyst. Electrochemical impedance spectroscopy (EIS) measurements further confirm the efficient mass transfer for Z8@DA-FIP-950-C. Fig. 4c shows the EIS Nyquist plots for Z8@DA-FIP-950-C and Z8@FIP-950-C at 1.2 A cm^{-2} , together with the model equivalent circuit. As can be seen, the Z8@DA-FIP-950-C cathode exhibited a smaller charge transfer resistance ($0.10 \Omega \text{ cm}^2$) compared to Z8@FIP-950-C ($0.13 \Omega \text{ cm}^2$). This is because the dense FeN_4 active sites, coupled with abundant mesopores and macropores, promoted the charge transfer and diffusion of O_2 to the active sites, contributing to the superior ORR activity and excellent fuel cell performance.

As is well-known, the overall ORR activity of Fe-N-C catalyst depends on the number of active sites [60,61]. However, few studies have correlated the quantitative gravimetric active site density (MSD) to the ORR activity for either the half-cell or single cell. To further study the

quantitative relationship of the active site and the catalytic activity, we quantitatively characterize the gravimetric active site density (MSD) for Z8@DA-FIP-950-C and Z8@FIP-950-C, which were then correlated to the current density measured by RDE and power density of the fuel cell (Figs. 4, S16, S25–S29, Tables S4, and S5). The MSD of the catalysts were quantified by the in-situ electrochemical adsorption-stripping experiments [30]. As shown in Fig. 4d, the FeN₄ MSD for both Z8@DA-FIP-950-C and Z8@FIP-950-C increased with increasing the FIP addition, and then leveled off at 63 and 37 $\mu\text{mol g}^{-1}$ when the FIP solution addition reached to 0.6 ml. Z8@DA-FIP-950-C showed a higher utilization of iron sources than Z8@FIP-950-C at any FIP addition, demonstrating the advantage for the presence of PDA to suppress the formation of Fe-based nanoparticles and generation of more FeN₄ sites for ORR. Fig. 4e shows the current densities at 0.8 V measured by RDE as a function of FeN₄ MSD, revealing a linear increase in current density with increasing FeN₄ MSD (5–37 $\mu\text{mol g}^{-1}$) for Z8@FIP-950-C. In contrast, Z8@DA-FIP-950-C shows an accelerating trend in high concentration region (above 42 $\mu\text{mol g}^{-1}$). Fig. 4f shows the correlation between the FeN₄ MSD and PEMFC power density at 0.5, 0.6, and 0.7 V, respectively. As can be seen, the PEMFC power densities of Z8@FIP-950-C increased slowly with increasing FeN₄ MSD, while the fuel cell power density of Z8@DA-FIP-950-C remarkably increased. We further correlated the ORR activity with PEMFC current densities at 0.7, 0.75, and 0.8 V (Fig. 4g). The PEMFC current densities of Z8@DA-FIP-950-C at the voltages shown in the figure show an exponential increase with increasing the ORR activity (i.e., FeN₄ MSD). The

related current densities of Z8@DA-FIP-950-C and Z8@FIP-950-C at different MSDs were summarized in Table S4. These results indicate the predominant role of the FeN₄ site density played in regulating the kinetic activity and the PEMFC power performance of the catalysts.

It is worth noting that the current densities measured by RDE at 0.8 V (Fig. 4e), the PEMFC power densities measured at various voltages shown in Fig. 4f, and the peak power densities (Fig. S29) for Z8@DA-FIP-950-C are all higher than those of Z8@FIP-950-C over the range of the FeN₄ MSD from 24 to 37 $\mu\text{mol g}^{-1}$. This is because abundant defective-edge FeN₄ sites formed in Z8@DA-FIP-950-C by C-N bond cleavage enriched the mesopores and macropores (Figs. S30 and S31), leading to the higher ORR activity for Z8@DA-FIP-950-C than that of the Z8@FIP-950-C. This is also confirmed by the higher average TOF (3.00 s^{-1}) for the defective-edge FeN₄ site of Z8@DA-FIP-950-C than that (2.85 s^{-1}) of Z8@FIP-950-C (Table S5). Indeed, an earlier report indicates that the defective-edge FeN₄ sites can easily form within the porous carbon structure [45].

We further measured the Z8@DA-FIP-950-C-based MEA in a fuel cell with air feeding to the cathode. As shown in Fig. 4h, Z8@DA-FIP-950-C displays an impressive peak power density of 454 mW cm^{-2} , reaching to about 77% of the maximum power density (591 mW cm^{-2}) of Pt/C-based MEA operated under the same conditions (Fig. S32). To the best of our knowledge, it is the first-rank power performance of H₂/air PEMFCs based on non-precious metal catalysts reported previously (Fig. 4i and Table S9). Moreover, the durability of the cathodes made with Z8@DA-FIP-950-C were tested under 2 bar H₂/O₂ and 1 bar H₂/air

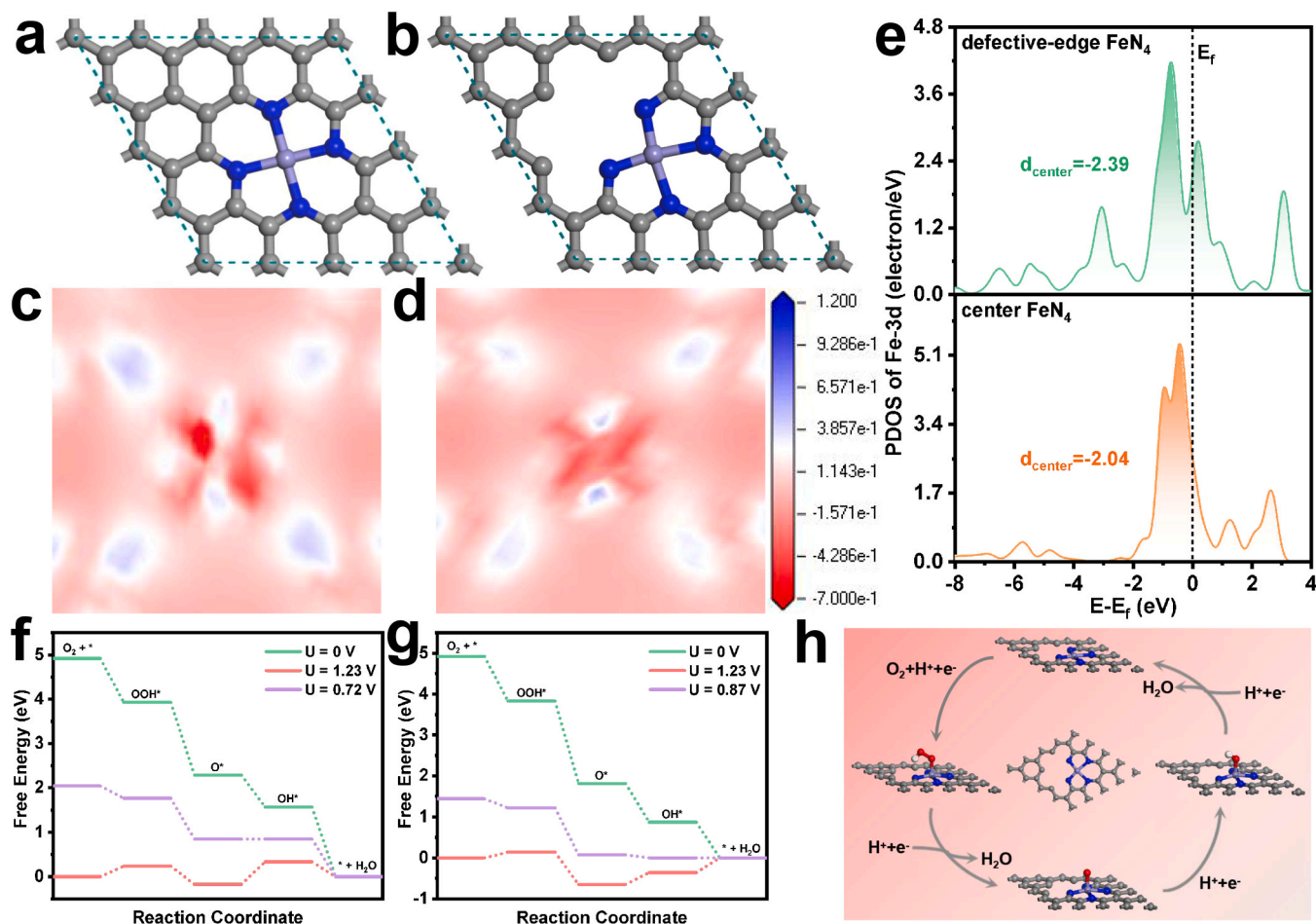


Fig. 5. Model structures used in theoretical studies: a) center and b) defective-edge FeN₄ structures. Calculated charge density differences for c) center and d) defective-edge FeN₄ models; blue and red areas represent charge density increase and decrease, respectively. Larger values represent increased electron density. e) PDOS of Fe 3d in the center and defective-edge FeN₄ models. ORR free-energy diagrams of the f) center and g) defective-edge FeN₄ models. h) Proposed ORR mechanism on the defective-edge FeN₄ site.

(Fig. S33). It can be seen that the H₂/air PEMFC stability of Z8@DA-FIP-950-C is superior even to the H₂/O₂ PEMFC of Z8@DA-FIP-950-C.

3.4. Insight of ORR process on Z8@DA-FIP-950-C catalyst with DFT simulation

To understand the intrinsic activity of the defective-edge FeN₄ sites introduced by the meso/macropores in Z8@DA-FIP-950-C, two FeN₄ models (center and defective-edge) with the typical four-electron transfer pathway toward ORR were proposed for DFT calculations (Fig. 5a,b). Fig. 5c,d show the charge density differences of the center and defective-edge FeN₄ sites. It can be observed that the electron density of Fe centered structure in center FeN₄ site is lower than that of defective-edge FeN₄ site, suggesting the weakened adsorption of ORR intermediates on the defective-edge FeN₄ active site in Z8@DA-FIP-950-C. The weakened adsorption result from the filled d-band of the Fe center with defective-edge, as also demonstrated by the down-shifted d-band center for the defective-edge FeN₄ model (Fig. 5e). From the viewpoint of thermodynamics, the weakened adsorption should be beneficial to ORR due to that the issue of too strong binding of ORR intermediates on the Fe center can be alleviated [62]. Fig. 5f,g show the Gibbs free-energy diagrams of the reduction of O₂ to H₂O on the center and defective-edge FeN₄ models. At zero electrode potential (U = 0 V versus reversible hydrogen electrode (RHE)), each ORR step for the two models is thermodynamically downslope, indicating all the elementary steps are exothermic. However, at the equilibrium potential (U = 1.23 V), several endothermic ORR steps occurred in the two models. It can be observed that the highest endothermic energy ($\Delta G_{\text{OH}^*} = 0.51$ eV) for the center FeN₄ model implies that the third electron-transfer step ($\text{O}^* + 2\text{H}^+ + 2\text{e}^- + \text{H}_2\text{O} \rightarrow \text{OH}^* + \text{H}^+ + \text{e}^- + \text{H}_2\text{O}$) is the rate-determining step (RDS) of ORR on the center FeN₄ model. By contrast, the highest endothermic energy for the defective-edge FeN₄ model was calculated to be 0.36 eV, and the corresponding RDS is the last electron-transfer step ($\text{OH}^* + \text{H}^+ + \text{e}^- + \text{H}_2\text{O} \rightarrow * + 2\text{H}_2\text{O}$). The lower endothermic energy of the RDS for the defective-edge FeN₄ model suggests that the defective-edge FeN₄ model possesses a lower activation energy barrier in comparison to the center FeN₄ model, and the center FeN₄ model shows more sluggish reaction dynamics. In addition, the thermodynamic limiting potential of the defective-edge FeN₄ model is up to 0.87 V, which is higher than that of the center FeN₄ model (0.72 V). This result further confirms that the defective-edge FeN₄ has a quite good catalytic activity toward ORR. The calculated free energy under various conditions were listed in Table S6, and the optimized atomic configurations of oxygen intermediates adsorbed on these two FeN₄ models were also presented in Fig. S34. The proposed mechanism of ORR on the defective-edge FeN₄ active site is depicted in Fig. 5h. The above calculated results show that the defective-edge FeN₄ sites at Z8@DA-FIP-950-C possess superior ORR catalytic activity, which is consistent with the above-mentioned experimental results.

4. Conclusion

In summary, we have developed a facile PDA-metal complex-assisted pyrolysis strategy for the fabrication of high-dense FeN₄ sites decorated hierarchical porous carbons without acid treatment. The as-prepared Z8@DA-FIP-950-C catalyst exhibited superior performance toward ORR in acidic medium, as good as the commercial Pt/C. Significantly, benefiting from the enriched triple-phase boundaries created by meso/macropores and highly exposed FeN₄ sites, the Z8@DA-FIP-950-C catalyst showed remarkable power performance for PEMFC, superior to most of the previously-reported non-precious metal catalysts. More importantly, we have established the relationship between the quantitative FeN₄ site density and ORR activity, and clearly found that the FeN₄ site density plays a crucial role in contributing to the half-cell and PEMFC performance. The excellent ORR intrinsic activity of defective-edge FeN₄ sites in Z8@DA-FIP-950-C has also been confirmed by the

DFT calculations. This work not only provides a new paradigm for the synthesis of highly efficient non-precious metal-based ORR catalysts for practical PEMFCs, but also paves a new way for the design and development of novel high-efficient single-atom catalysts without acid treatment for renewable energy technologies.

CRediT authorship contribution statement

Feng Liu: Conceptualization, Investigation, Methodology, Writing – original draft. **Lei Shi:** Writing – review & editing. **Xuanni Lin:** Writing – review & editing. **Donglin Yu:** Writing – review & editing. **Cai Zhang:** Writing – review & editing. **Rui Xu:** Writing – review & editing. **Dong Liu:** Project administration, Supervision, Writing – review & editing. **Jieshan Qiu:** Writing – review & editing. **Liming Dai:** Conceptualization, Supervision, Writing – review & editing. All authors discussed the results and commented on the article.

Declaration of Competing Interest

We declare that we have no known competing financial interests or personal relationships that could have appeared to influence the work reported in this paper.

Acknowledgements

This work was financially supported by the National Key Research and Development Program of China (2017YFA0206500), the Key Program of National Natural Science Foundation of China (51732002), the Distinguished Scientist Program at BUCT (buctylxj02), and the Fundamental Research Funds for the Central Universities (buctrc202007).

Appendix A. Supplementary material

Supplementary data associated with this article can be found in the online version at doi:10.1016/j.apcatb.2021.120860.

References

- [1] G. Wu, K.L. More, C.M. Johnston, P. Zelenay, High-performance electrocatalysts for oxygen reduction derived from polyaniline, iron, and cobalt, *Science* 332 (2011) 443–447, <https://doi.org/10.1126/science.1200832>.
- [2] K. Wang, H. Chen, X. Zhang, Y. Tong, S. Song, P. Tsiakaras, Y. Wang, Iron oxide@graphitic carbon core-shell nanoparticles embedded in ordered mesoporous N-doped carbon matrix as an efficient cathode catalyst for PEMFC, *Appl. Catal. B: Environ.* 264 (2020), 118468, <https://doi.org/10.1016/j.apcatb.2019.118468>.
- [3] M. Shao, Q. Chang, J.-P. Dodelet, R. Chenitz, Recent advances in electrocatalysts for oxygen reduction reaction, *Chem. Rev.* 116 (2016) 3594–3657, <https://doi.org/10.1021/acs.chemrev.5b00462>.
- [4] R. Sharma, S.M. Andersen, An opinion on catalyst degradation mechanisms during catalyst support focused accelerated stress test (AST) for proton exchange membrane fuel cells (PEMFCs), *Appl. Catal. B: Environ.* 239 (2018) 636–643, <https://doi.org/10.1016/j.apcatb.2018.08.045>.
- [5] M. Qiao, Y. Wang, Q. Wang, G. Hu, X. Mamat, S. Zhang, S. Wang, Hierarchically ordered porous carbon with atomically dispersed FeN₄ for ultraefficient oxygen reduction reaction in proton-exchange membrane fuel cells, *Angew. Chem. Int. Ed.* 59 (2020) 2688–2694, <https://doi.org/10.1002/anie.201914123>.
- [6] A. Brouzgou, S.Q. Song, P. Tsiakaras, Low and non-platinum electrocatalysts for PEMFCs: current status, challenges and prospects, *Appl. Catal. B: Environ.* 127 (2012) 371–388, <https://doi.org/10.1016/j.apcatb.2012.08.031>.
- [7] K. Gong, F. Du, Z. Xia, M. Durstock, L. Dai, Nitrogen-doped carbon nanotube arrays with high electrocatalytic activity for oxygen reduction, *Science* 323 (2009) 760–764, <https://doi.org/10.1126/science.1168049>.
- [8] T. Palaniselvam, V. Kashyap, S.N. Bhang, J.B. Baek, S. Kurungot, Nanoporous graphene enriched with Fe/Co-N active sites as a promising oxygen reduction electrocatalyst for anion exchange membrane fuel cells, *Adv. Funct. Mater.* 26 (2016) 2150–2162, <https://doi.org/10.1002/adfm.201504765>.
- [9] C.C. Hou, L. Zou, L. Sun, K. Zhang, Z. Liu, Y. Li, C. Li, R. Zou, J. Yu, Q. Xu, Single-atom iron catalysts on overhang-eave carbon cages for high-performance oxygen reduction reaction, *Angew. Chem. Int. Ed.* 59 (2020) 7384–7389, <https://doi.org/10.1002/ange.202002665>.
- [10] L. Chen, X. Liu, L. Zheng, Y. Lia, X. Guo, X. Wan, Q. Liu, J. Shang, J. Shui, Insights into the role of active site density in the fuel cell performance of Co-N-C catalysts,

- Appl. Catal. B: Environ. 256 (2019), 117849, <https://doi.org/10.1016/j.apcatb.2019.117849>.
- [11] M. Xiao, Y. Chen, J. Zhu, H. Zhang, X. Zhao, L. Gao, X. Wang, J. Zhao, J. Ge, Z. Jiang, S. Chen, C. Liu, W. Xing, Climbing the apex of the ORR volcano plot via binuclear site construction: electronic and geometric engineering, *J. Am. Chem. Soc.* 141 (2019) 17763–17770, <https://doi.org/10.1021/jacs.9b08362>.
 - [12] L. Jiao, H.L. Jiang, Metal-organic-framework-based single-atom catalysts for energy applications, *Chem* 5 (2019) 786–804, <https://doi.org/10.1016/j.chempr.2018.12.011>.
 - [13] X. Yang, Y. Wang, G. Zhang, L. Du, L. Yang, M. Markiewicz, J.-Y. Choi, R. Chenitz, S. Sun, SiO₂-Fe/N/C catalyst with enhanced mass transport in PEM fuel cells, *Appl. Catal. B: Environ.* 264 (2020), 118523, <https://doi.org/10.1016/j.apcatb.2019.118523>.
 - [14] D.-H. Kwak, S.-B. Han, D.-H. Kim, J.-E. Won, K.-W. Park, Amino acid-derived non-precious catalysts with excellent electrocatalytic performance and methanol tolerance in oxygen reduction reaction, *Appl. Catal. B: Environ.* 238 (2018) 93–103, <https://doi.org/10.1016/j.apcatb.2018.07.013>.
 - [15] R. Ma, Y. Zhou, C. Hu, M. Yang, F. Wang, K. Yan, Q. Liu, J. Wang, Post iron-doping of activated nitrogen-doped carbon spheres as a high-activity oxygen reduction electrocatalyst, *Energy Storage Mater.* 13 (2018) 142–150, <https://doi.org/10.1016/j.ensm.2018.01.008>.
 - [16] Y. Chen, S. Ji, Y. Wang, J. Dong, W. Chen, Z. Li, R. Shen, L. Zheng, Z. Zhuang, D. Wang, Y. Li, Isolated single iron atoms anchored on N-doped porous carbon as an efficient electrocatalyst for the oxygen reduction reaction, *Angew. Chem. Int. Ed.* 56 (2017) 6937–6941, <https://doi.org/10.1002/ange.201702473>.
 - [17] A. Zitolo, V. Goellner, V. Armel, M.-T. Sougrati, T. Mineva, L. Stievano, E. Fonda, F. Jaouen, Identification of catalytic sites for oxygen reduction in iron- and nitrogen-doped graphene materials, *Nat. Mater.* 14 (2015) 937–942, <https://doi.org/10.1038/nmat4367>.
 - [18] J. Li, S. Ghoshal, W. Liang, M.-T. Sougrati, F. Jaouen, B. Halevi, S. McKinney, G. McCool, C. Ma, X. Yuan, Z.-F. Ma, S. Mukerjee, Q. Jia, Structural and mechanistic basis for the high activity of Fe-N-C catalysts toward oxygen reduction, *Energy Environ. Sci.* 9 (2016) 2418–2432, <https://doi.org/10.1039/C6EE01160H>.
 - [19] Z. Li, L. Wei, W.-J. Jiang, Z. Hu, H. Luo, W. Zhao, T. Xu, W. Wu, M. Wu, J.-S. Hu, Chemical state of surrounding iron species affects the activity of Fe-Nx for electrocatalytic oxygen reduction, *Appl. Catal. B: Environ.* 251 (2019) 240–246, <https://doi.org/10.1016/j.apcatb.2019.03.046>.
 - [20] R. Ma, G. Lin, Q. Ju, W. Tang, G. Chen, Z. Chen, Q. Liu, M. Yang, Y. Lu, J. Wang, Edge-sited Fe-N₄ atomic species improve oxygen reduction activity via boosting O₂ dissociation, *Appl. Catal. B: Environ.* 265 (2020), 118593, <https://doi.org/10.1016/j.apcatb.2020.118593>.
 - [21] G. Wu, Current challenge and perspective of PGM-free cathode catalysts for PEM fuel cells, *Front. Energy* 11 (2017) 286–298, <https://doi.org/10.1007/s11708-017-0477-3>.
 - [22] X. Wan, X. Liu, Y. Li, R. Yu, L. Zheng, W. Yan, H. Wang, M. Xu, J. Shui, Fe-N-C electrocatalyst with dense active sites and efficient mass transport for high-performance proton exchange membrane fuel cells, *Nat. Catal.* 2 (2019) 259–268, <https://doi.org/10.1038/s41929-019-0237-3>.
 - [23] X. Fu, G. Jiang, G. Wen, R. Gao, S. Li, M. Li, J. Zhu, Y. Zheng, Z. Li, Y. Hu, L. Yang, Z. Bai, A. Yu, Z. Chen, Densely accessible Fe-N_x active sites decorated mesoporous carbon-spheres for oxygen reduction towards high performance aluminum-air flow batteries, *Appl. Catal. B: Environ.* 293 (2021), 120176, <https://doi.org/10.1016/j.apcatb.2021.120176>.
 - [24] K. Singh, F. Razmjooei, J.-S. Yu, Active sites and factors influencing them for efficient oxygen reduction reaction in metal-N coordinated pyrolyzed and non-pyrolyzed catalysts: a review, *J. Mater. Chem. A* 5 (2017) 20095–20119, <https://doi.org/10.1039/C7TA05222G>.
 - [25] J. Han, H. Bao, J.-Q. Wang, L. Zheng, S. Sun, Z.L. Wang, C. Sun, 3D N-doped ordered mesoporous carbon supported single-atom Fe-N-C catalysts with superior performance for oxygen reduction reaction and zinc-air battery, *Appl. Catal. B: Environ.* 280 (2021), 119411, <https://doi.org/10.1016/j.apcatb.2020.119411>.
 - [26] Z. Yang, Y. Wang, M. Zhu, Z. Li, W. Chen, W. Wei, T. Yuan, Y. Qu, Q. Xu, C. Zhao, X. Wang, P. Li, Y. Li, Y. Wu, Y. Li, Boosting oxygen reduction catalysis with Fe-N₄ Sites decorated porous carbons toward fuel cells, *ACS Catal.* 9 (2019) 2158–2163, <https://doi.org/10.1021/acscatal.8b04381>.
 - [27] L. Yang, D. Cheng, X. Zeng, X. Wan, J. Shui, Z. Xiang, D. Cao, Unveiling the high-activity origin of single-atom iron catalysts for oxygen reduction reaction, *Proc. Natl. Acad. Sci. USA* 115 (2018) 6626–6631, <https://doi.org/10.1073/pnas.1800771115>.
 - [28] X. Ao, W. Zhang, Z. Li, J.-G. Li, L. Soule, X. Huang, W.-H. Chiang, H.M. Chen, C. Wang, M. Liu, X.C. Zeng, Markedly enhanced oxygen reduction activity of single-atom Fe catalysts via integration with Fe nanoclusters, *ACS Nano* 13 (2019) 11853–11862, <https://doi.org/10.1021/acsnano.9b05913>.
 - [29] I. Martinaiou, A.H.A.M. Videla, N. Weidler, M. Kübler, W.D.Z. Wallace, S. Paul, S. Wagner, A. Shahraei, R.W. Stark, S. Specchia, U.I. Kramm, Activity and degradation study of an Fe-N-C catalyst for ORR in direct methanol fuel cell (DMFC), *Appl. Catal. B: Environ.* 262 (2020), 118217, <https://doi.org/10.1016/j.apcatb.2019.118217>.
 - [30] D. Malko, A. Kucernak, T. Lopes, In situ electrochemical quantification of active sites in Fe-N/C non-precious metal catalysts, *Nat. Commun.* 7 (2016) 13285, <https://doi.org/10.1038/ncomms13285>.
 - [31] B. Delley, From molecules to solids with the DMol3 approach, *J. Chem. Phys.* 113 (2000) 7756–7764, <https://doi.org/10.1063/1.1316015>.
 - [32] S. Grimme, J. Antony, S. Ehrlich, H. Krieg, A consistent and accurate ab initio parametrization of density functional dispersion correction (DFT-D) for the 94 elements H-Pu, *J. Chem. Phys.* 132 (2010), 154104, <https://doi.org/10.1063/1.3382344>.
 - [33] X. Fu, N. Li, B. Ren, G. Jiang, Y. Liu, F.M. Hassan, D. Su, J. Zhu, L. Yang, Z. Bai, Z. P. Cano, A. Yu, Z. Chen, Tailoring FeN₄ sites with edge enrichment for boosted oxygen reduction performance in proton exchange membrane fuel cell, *Adv. Energy Mater.* 9 (2019), 1803737, <https://doi.org/10.1002/aenm.201803737>.
 - [34] X. Wang, Y. Jia, X. Mao, D. Liu, W. He, J. Li, J. Liu, X. Yan, J. Chen, L. Song, A. Du, X. Yao, Edge-rich Fe-N₄ active sites in defective carbon for oxygen reduction catalysis, *Adv. Mater.* 32 (2020), 2000966, <https://doi.org/10.1002/adma.202000966>.
 - [35] J.K. Norskov, J. Rossmeisl, A. Logadottir, L. Lindqvist, J.R. Kitchin, T. Bligaard, H. Jonsson, Origin of the overpotential for oxygen reduction at a fuel-cell cathode, *J. Phys. Chem. B* 108 (2004) 17886–17892, <https://doi.org/10.1021/jp047349j>.
 - [36] X. Jiang, S. Li, Y. Bai, L. Shao, Ultra-facile aqueous synthesis of nanoporous zeolitic imidazolate framework membranes for hydrogen purification and olefin/paraffin separation, *J. Mater. Chem. A* 7 (2019) 10898–10904, <https://doi.org/10.1039/C8TA11748A>.
 - [37] R. Jiang, L. Li, T. Sheng, G. Hu, Y. Chen, L. Wang, Edge-site engineering of atomically dispersed Fe-N₄ by selective C–N bond cleavage for enhanced oxygen reduction reaction activities, *J. Am. Chem. Soc.* 140 (2018) 11594–11598, <https://doi.org/10.1021/jacs.8b07294>.
 - [38] X. Wang, Y. Jia, X. Mao, L. Zhang, D. Liu, L. Song, X. Yan, J. Chen, D. Yang, J. Zhou, K. Wang, A. Du, X. Yao, A directional synthesis for topological defect in carbon, *Chem* 6 (2020) 2009–2023, <https://doi.org/10.1016/j.chempr.2020.05.010>.
 - [39] D. Li, Y. Jia, G. Chang, J. Chen, H. Liu, J. Wang, Y. Hu, Y. Xia, D. Yang, X. Yao, A defect-driven metal-free electrocatalyst for oxygen reduction in acidic electrolyte, *Chem* 4 (2018) 2345–2356, <https://doi.org/10.1016/j.chempr.2018.07.005>.
 - [40] H. Zhao, C. Sun, Z. Jin, D.-W. Wang, X. Yan, Z. Chen, G. Zhu, X. Yao, Carbon for the oxygen reduction reaction: a defect mechanism, *J. Mater. Chem. A* 3 (2015) 11736–11739, <https://doi.org/10.1039/C5TA02229K>.
 - [41] M.-J. Wang, Z.X. Mao, L. Liu, L. Peng, N. Yang, J. Deng, W. Ding, J. Li, Z. Wei, Preparation of hollow nitrogen doped carbon via stresses induced orientation contraction, *Small* 14 (2018), 1804183, <https://doi.org/10.1002/smll.201804183>.
 - [42] M. Xiao, J. Zhu, L. Ma, Z. Jin, J. Ge, X. Deng, Y. Hou, Q. He, J. Li, Q. Jia, S. Mukerjee, R. Yang, Z. Jiang, D. Su, C. Liu, W. Xing, Microporous framework induced synthesis of single-atom dispersed Fe-N-C acidic ORR catalyst and its in situ reduced Fe-N₄ active site identification revealed by X-ray absorption spectroscopy, *ACS Catal.* 8 (2018) 2824–2832, <https://doi.org/10.1021/acscatal.8b00138>.
 - [43] Y. Bian, H. Wang, J. Hu, B. Liu, D. Liu, L. Dai, Nitrogen-rich holey graphene for efficient oxygen reduction reaction, *Carbon* 162 (2020) 66–73, <https://doi.org/10.1016/j.carbon.2020.01.110>.
 - [44] J. Wang, W. Liu, G. Luo, Z. Li, C. Zhao, H. Zhang, M. Zhu, Q. Xu, X. Wang, C. Zhao, Y. Qu, Z. Yang, T. Yao, Y. Li, Y. Lin, Y. Wu, Y. Li, Synergistic effect of well-defined dual sites boosting the oxygen reduction reaction, *Energy Environ. Sci.* 11 (2018) 3375–3379, <https://doi.org/10.1039/C8EE02656D>.
 - [45] H.T. Chung, D.A. Cullen, D. Higgins, B.T. Sneed, E.F. Holby, K.L. More, P. Zelenay, Direct atomic-level insight into the active sites of a high-performance PGM-free ORR catalyst, *Science* 357 (2017) 479–483, <https://doi.org/10.1126/science.aan2255>.
 - [46] F. Jaouen, J. Herranz, M. Lefevre, J.P. Dodelet, U.I. Kramm, I. Herrmann, P. Bogdanoff, J. Maruyama, T. Nagaoka, A. Garsuch, J.R. Dahn, T. Olson, S. Pylypenko, P. Atanassov, E.A. Ustinov, Cross-laboratory experimental study of non-noble-metal electrocatalysts for the oxygen reduction reaction, *ACS Appl. Mater. Interfaces* 1 (2009) 1623–1639, <https://doi.org/10.1021/am900219g>.
 - [47] S. Yang, Y. Yu, M. Dou, Z. Zhang, L. Dai, F. Wang, Two-dimensional conjugated aromatic networks as high-site-density and single-atom electrocatalysts for the oxygen reduction reaction, *Angew. Chem. Int. Ed.* 58 (2019) 14724–14730, <https://doi.org/10.1002/anie.201908023>.
 - [48] Y. Pan, S. Liu, K. Sun, X. Chen, B. Wang, K. Wu, X. Cao, W.-C. Cheong, R. Shen, A. Han, Z. Chen, L. Zheng, J. Luo, Y. Lin, Y. Liu, D. Wang, Q. Peng, Q. Zhang, C. Chen, Y. Li, A bimetallic Zn/Fe polyphthalocyanine-derived single-atom Fe-N₄ catalytic site: a superior trifunctional catalyst for overall water splitting and Zn-Air batteries, *Angew. Chem. Int. Ed.* 57 (2018) 8614–8618, <https://doi.org/10.1002/anie.201804349>.
 - [49] Y. Chen, S. Ji, S. Zhao, W. Chen, J. Dong, W.-C. Cheong, R. Shen, X. Wen, L. Zheng, A.I. Rykov, S. Cai, H. Tang, Z. Zhuang, C. Chen, Q. Peng, D. Wang, Y. Li, Enhanced oxygen reduction with single-atomic-site iron catalysts for a zinc-air battery and hydrogen-air fuel cell, *Nat. Commun.* 9 (2018) 5422, <https://doi.org/10.1038/s41467-018-07850-2>.
 - [50] Y. Pan, Y. Chen, K. Wu, Z. Chen, S. Liu, X. Cao, W.-O. Cheong, T. Meng, J. Luo, L. Zheng, C. Liu, D. Wang, Q. Peng, J. Li, C. Chen, Regulating the coordination structure of single-atom Fe-N₄C_y catalytic sites for benzene oxidation, *Nat. Commun.* 10 (2019) 4290, <https://doi.org/10.1038/s41467-019-12362-8>.
 - [51] P. Yin, T. Yao, Y. Wu, L. Zheng, Y. Lin, W. Liu, H. Ju, J. Zhu, X. Hong, Z. Deng, G. Zhou, S. Wei, Y. Li, Single cobalt atoms with precise N-coordination as superior oxygen reduction reaction catalysts, *Angew. Chem. Int. Ed.* 55 (2016) 10800–10805, <https://doi.org/10.1002/ange.201604802>.
 - [52] U.I. Kramm, M. Lefevre, N. Larouche, D. Schmeisser, J.-P. Dodelet, Correlations between mass activity and physicochemical properties of Fe/N/C catalysts for the ORR in PEM fuel cell via ⁵⁷Fe Mössbauer spectroscopy and other techniques, *J. Am. Chem. Soc.* 136 (2014) 978–985, <https://doi.org/10.1021/ja410076f>.
 - [53] H. Chen, S. You, Y. Ma, C. Zhang, B. Jing, Z. Cai, B. Tang, N. Ren, J. Zou, Carbon thin-layer-protected active sites for ZIF-8-derived Nitrogen-enriched carbon

- frameworks/expanded graphite as metal-free catalysts for oxygen reduction in acidic media, *Chem. Mater.* 30 (2018) 6014–6025, <https://doi.org/10.1021/acs.chemmater.8b02275>.
- [54] F. Liu, L. Shi, S. Song, K. Ge, X. Zhang, Y. Guo, D. Liu, Simultaneously engineering the coordination environment and pore architecture of metal-organic framework-derived single atomic iron catalysts for ultraefficient oxygen reduction, *Small* 17 (2021), 2102425, <https://doi.org/10.1002/sml.202102425>.
- [55] S. Zhang, H. Xue, W.-l Li, J. Sun, N. Guo, T. Song, H. Dong, J. Zhang, X. Ge, W. Zhang, Q. Wang, Constructing precise coordination of nickel active sites on hierarchical porous carbon framework for superior oxygen reduction, *Small* 17 (2021), 2102125, <https://doi.org/10.1002/sml.202102125>.
- [56] Y. Guo, F. Liu, L. Feng, X. Wang, X. Zhang, J. Liang, Single Co atoms anchored on nitrogen-doped hierarchically ordered porous carbon for selective hydrogenation of quinolines and efficient oxygen reduction, *Chem. Eng. J.* 429 (2022), 132150, <https://doi.org/10.1016/j.cej.2021.132150>.
- [57] X. Xie, C. He, B. Li, Y. He, D.A. Cullen, E.C. Wegener, A.J. Kropf, U. Martinez, Y. Cheng, M.H. Engelhard, M.E. Bowden, M. Song, T. Lemmon, X.S. Li, Z. Nie, J. Liu, D.J. Myers, P. Zelenay, G. Wang, G. Wu, V. Ramani, Y. Shao, Performance enhancement and degradation mechanism identification of a single-atom Co-N-C catalyst for proton exchange membrane fuel cells, *Nat. Catal.* 3 (2020) 1044–1054, <https://doi.org/10.1038/s41929-020-00546-1>.
- [58] Y. Chen, R. Gao, S. Ji, H. Li, K. Tang, P. Jiang, H. Hu, Z. Zhang, H. Hao, Q. Qu, X. Liang, W. Chen, J. Dong, D. Wang, Y. Li, Atomic-level modulation of electronic density at cobalt single-atom sites derived from metal-organic frameworks: enhanced oxygen reduction performance, *Angew. Chem. Int. Ed.* 60 (2021) 3212–3221, <https://doi.org/10.1002/anie.202012798>.
- [59] J. Hu, D. Wu, C. Zhu, C. Hao, C. Xin, J. Zhang, J. Guo, N. Li, G. Zhang, Y. Shi, Melt-salt-assisted direct transformation of solid oxide into atomically dispersed FeN₄ sites on nitrogen-doped porous carbon, *Nano Energy* 72 (2020), 104670, <https://doi.org/10.1016/j.nanoen.2020.104670>.
- [60] H. Fei, J. Dong, Y. Feng, C. Allen, C. Wan, B. Voloskiy, M. Li, Z. Zhao, Y. Wang, H. Sun, P. An, W. Chen, Z. Guo, C. Lee, D. Chen, I. Shakir, M. Liu, T. Hu, Y. Li, A. I. Kirkland, X. Duan, Y. Huang, General synthesis and definitive structural identification of MN₄C₄ single-atom catalysts with tunable electrocatalytic activities, *Nat. Catal.* 1 (2018) 63–72, <https://doi.org/10.1038/s41929-017-0008-y>.
- [61] Q. Liu, X. Liu, L. Zheng, J. Shui, The solid-phase synthesis of an Fe-N-C electrocatalyst for high-power proton-exchange membrane fuel cells, *Angew. Chem. Int. Ed.* 57 (2018) 1204–1208, <https://doi.org/10.1002/ange.201709597>.
- [62] F. Wang, Y. Zhou, S. Lin, L. Yang, Z. Hu, D. Xie, Axial ligand effect on the stability of Fe-N-C electrocatalysts for acidic oxygen reduction reaction, *Nano Energy* 78 (2020), 105128, <https://doi.org/10.1016/j.nanoen.2020.105128>.